Nanoscale Advances

ROYAL SOCIETY OF CHEMISTRY

PAPER

View Article Online
View Journal | View Issue

Cite this: *Nanoscale Adv.*, 2022, **4**, 200

Regulation of photo triggered cytotoxicity in electrospun nanomaterials: role of photosensitizer binding mode and polymer identity†

Anzhela Galstyan, *[a] Hussaini Majiya [b] and Urlich Dobrindt[c]

Received 27th September 2021
Accepted 8th November 2021

DOI: 10.1039/d1na00717c

rsc.li/nanoscale-advances

Although electrospun nanomaterials containing photoactive dyes currently compete with the present state of art antimicrobial materials, relatively few structure–activity relationships have been established to identify the role of carrier polymer and photosensitizer binding mode on the performance of the materials. In this study scaffolds composed of poly(vinyl alcohol), polyacrylonitrile, poly(caprolactone), and tailor-made phthalocyanine-based photosensitizers are developed utilizing electrospinning as a simple, time and cost-effective method. The photoinduced activity of nanofibrous materials was characterized *in vitro* against *E. coli* and *B. subtilis* as models for Gram-negative and Gram-positive bacteria respectively, as well as against bacteriophages phi6 and MS2 as models for enveloped and non-enveloped viruses respectively. For the first time, we show how polymer-specific properties affect antifouling and antimicrobial activity of the nanofibrous material, indicating that the most promising way to increase efficiency is likely *via* methods that focus on increasing the number of short, but strong and reversible bacteria–surface interactions.

1. Introduction

The demand for functional antimicrobial surfaces and interfaces is increasing rapidly in different fields of medicine and biotechnology,[1,2] including agricultural and food packaging industries. Recently the research on multifunctional materials has attracted increasing attention for protective clothing applications; the COVID-19 pandemic has demonstrated the importance of interfaces with advanced features.[3] To improve the antimicrobial efficiency *in situ* different materials were developed. In general, they can be categorized into leaching and non-leaching materials, which is essential for a particular application in the medical, hygiene-sensitive, and environmental fields. One of the widely employed strategies is the introduction of metals such as Ag,[4] Cu[5] or metal-based nanoparticles such Fe_3O_4 (ref. 6) or TiO_2 (ref. 7) into the material. A disadvantage of this strategy is that these materials might spread toxic compounds in the environment and contribute to the development of resistance.[8,9] Another widely applied strategy is using surface-grafted antimicrobial moieties such as quaternary ammonium compounds.[10] Though these systems have gained significant scientific attention, recent studies showed that at sub-inhibitory concentrations antimicrobial resistance can occur.[11,12] One alternative approach with the potential to generate environmentally friendly self-cleaning coating materials is the use of photosensitization-based inactivation methods.[13,14] Materials based on photodynamic action can inactivate bacteria and viruses in a very short time and thus prevent the further spread of pathogens and the development of resistance.

Nano- and micro-sized fibers are very attractive materials for the construction of antimicrobial surfaces and interfaces and could be generated by electrospinning, which is a low cost and simple technique suitable for large-scale production.[15] Electrospun materials can be obtained from a rich variety of polymers and are widely used in environmental and clinical applications.[16,17] The common application fields are water and air filtration (*e.g.* facial mask[18] or advanced high-efficiency particulate air – HEPA filters[19]), catalysis,[20] energy harvesting and storage.[21,22] For fabrication of mechanically robust systems polyacrylonitrile (PAN), polystyrene (PS), poly (vinyl alcohol) (PVA), polyvinylpyrrolidone (PVP), *etc.* have been used for electrospinning. For instance, in their recent study, Liu *et al.*[23] developed lightweight air filters composed of different polymers, showing that electrospun PAN nanofibers (NFs) with *ca.* 200 nm diameter were the most effective in the filtration of particulate matter. Hydrophilic polymers, such as PVA and polyacrylic acid (PAA) have been shown to hinder the leaching of metallic nanoparticles and are one of the preferred carriers

[a]*Center for Soft Nanoscience Westfälische Wilhelms-Universität Münster, Busso-Peus-Strasse 10, 48149 Münster, Germany. E-mail: anzhela.galstyan@wwu.de*
[b]*Department of Microbiology, Ibrahim Badamasi Babangida University, KM3 Lapai-Minna Road, P.M.B 11, Lapai, Nigeria*
[c]*Institut of Hygiene, Westfälische Wilhelms-Universität Münster, Mendelstrasse 7, 48149 Münster, Germany*

† Electronic supplementary information (ESI) available. See DOI: 10.1039/d1na00717c

for the fabrication of electrospun NFs used in water disinfection.[24] Nevertheless, due to the mechanical and chemical stability, PAN is the most used polymer in this field.[25]

Electrospun NFs can mimic extracellular matrix and have been also extensively explored as scaffolds for tissue engineering.[26,27] For instance, materials based on biocompatible polymers such as poly(ε-caprolactone) (PCL) and poly L-lactic acid (PLLA) were found to be suitable for tissue-engineered heart valves.[28] Numerous studies also confirmed the suitability of electrospun scaffolds for skin regeneration and wound therapeutics.[29,30] For instance, it was shown that electrospun chitosan-PCL scaffold could promote more complete wound closure than commercially available Tegaderm dressing.[31] Nevertheless, it is important to note that in most studies an important function of preventing bacterial growth or infection is often missing.[32]

Many different systems with encapsulated or attached photosensitizers (PS) have been developed to achieve photo-triggered inactivation of microorganisms. Although numerous PSs are featured by strong antimicrobial activity, the activity of PS implemented in or bound to NFs is still largely unverified and the requirements for effective antimicrobial action remain controversial. Also, the influence of the inherent material properties on the fouling behavior has not yet been sufficiently explored. Surface biofouling caused by the unspecific adsorption of proteins, bacteria, or cells is an urgent challenge that diminishes the performance of the material contributing to the formation the biofilms and secondary infections.[33–36] Targeted design of polymeric nanomaterials with predictable and controllable properties is necessary to achieve effective light-controlled disinfection and meet requirements for future clinical and biotechnological applications. Properties of this unique class of materials could be modulated at several sites; (i) varying PS, (ii) varying binding mode of PS, (iii) using different carrier polymers or mixtures of them, or (iv) using additional cross-linking or functionalization of the polymers. Additionally, electrospinning parameters could also be modulated to reach the desired outcome.

In this study, the antimicrobial and antifouling efficiency of NFs that contain implemented or covalently bound PS and PVA, PAN, or PCL as carrier polymers have been investigated quantitatively *in vitro* in direct comparison to determine how the composition of the material can predictably modulate dye performance (Fig. 1). Our results contribute to a fundamental understanding of the structure–activity relationship of the nanofiber-based photoactive materials and create new opportunities for the development of innovative disinfection strategies combining light and nanotechnology.

2. Results and discussion

2.1 Synthesis and characterization of photosensitizers

To demonstrate significance of encapsulated *vs.* covalently bound PS a symmetric phthalocyanine (**SymPc**) containing four quaternized 4-pyridylsulfanyl units and asymmetric phthalocyanine containing three quaternized 4-pyridylsulfanyl units and a single anchoring group (**AsymPc**) were synthesized.

Precursors of PSs were obtained following our previously published method *via* mixed cyclization of 2-mercaptopyridine and 3-(2-{2-[2-(2-hydroxyethoxy)ethoxy]ethoxy}-ethoxy)phthalonitrile in a molar ratio of 1 : 5 in the presence of $Zn(OAc)_2 \cdot 2H_2O$ and 1,8-diazabicyclo[5.4.0.]undec-7-ene in *n*-pentanol. After column chromatographic separation, Pc with low symmetry was reacted with succinic anhydride to introduce carboxylic acid functionality for the further coupling reaction. Finally, both Pcs were quaternized using methylene iodide leading to the formation of water soluble **SymPc** and **AsymPc**. Both of them have been fully characterized by ^{1}H NMR technique and high-resolution mass spectrometry (see the ESI† for details).

As a common feature, Pc-based dyes are very robust, have significant molar absorption coefficients in the near-infrared region and high yield of ROS generation.[13] Photophysical properties of **SymPc** and **AsymPc** were studied in DMF and H_2O and important data are summarized in Table 1. Both PSs exhibit characteristic absorbance in the B- and Q-band regions. The substitution pattern has almost no effect on the maximum absorbance and emission of PSs in DMF, however, slightly different behavior for absorption in H_2O was observed, indicating an influence of the polyethylene glycol in **AsymPc** on the solubility of the molecule. Overall the absorption intensity in H_2O was weakened as compared to that of DMF due to the quenching caused by self-aggregation (Fig. S1 and S2, ESI†). Self-assembly of PS into photoactive J-type aggregate (characterized through red-shifted wavelengths) and photoinactive H-type aggregate (characterized through blue-shifted wavelengths) play a fundamental role in understanding its photophysical features. As shown in Fig. 2, UV-vis spectra of both PS in H_2O show transitions characteristic of both H-type aggregates and monomers. Although the spectral differentiation between the H-aggregates and monomeric species is not straightforward because of the overlap of the spectra, it is obvious that **SymPc** forms larger numbers of H-aggregates than **AsymPc**. Nevertheless, switching between H- or J-type aggregates and monomers is possible when the environment of PS is altered, *e.g.*, by incorporation into polymers (*vide infra*) or when bound to the microorganisms.[37] The relative orientation of the transition dipole moments of neighboring molecules is largely determined by the π–π stacking between Pc macrocycles, but hydrophilic/hydrophobic, electrostatic, and in certain cases more specific interactions such as metal–ligand coordination between PSs and/or components in the environment also play an important role.

The ability to produce ROS is a crucial factor that must be addressed for a PS used in aPDT. ROS generation ability of **SymPc** and **AsymPc** was assessed in DMF and H_2O using unsubstituted zinc(II)phthalocyanine or methylene blue as standard and diphenylisobenzofuran (DPBF) or 2′,7′-dichlorofluorescein diacetate (DCFDA) as ROS sensitive agent (Fig. S3 and S4, ESI†). Consistent with their structural differences PSs differ in their capability to generate ROS under near-infrared light irradiation. Φ_Δ in DMF were determined to be 0.41 and 0.60 and in H_2O 0.26 and 0.14 for **SymPc** and **AsymPc**, correspondingly. Although **SymPc** presented a broader and blue-shifted absorption in H_2O, its ROS generation was somehow

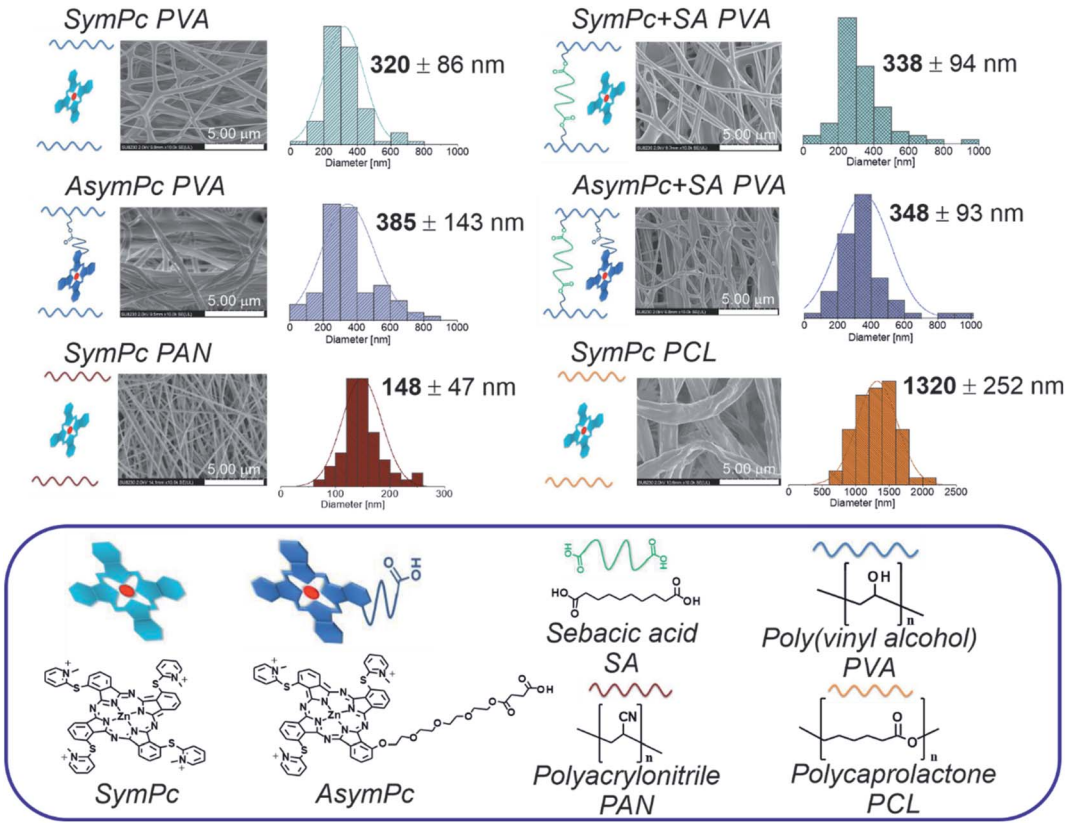

Fig. 1 Schematic illustration of the composition, morphology and diameter distribution of electrospun nanofiber membranes used in this study.

higher. We assume that the two PSs form different types of aggregates determined not only by repulsion between positively charged pyridinium units but also, more importantly, by solvophobic forces,[38] in which the polyethylene glycol substituent may play an important role. Overall, the high ROS generating ability and positive charge of both PSs points to great potential for a broad spectrum of antibacterial and antiviral activity.

2.2 Fabrication and characterization of NFs

In this study, PVA, PAN, and PCL were used as carrier polymers for the fabrication of the nanofibrous membranes. PVA is one of the most widely used polymers in the biomedical field due to its properties such as biocompatibility, biodegradability, mechanical resistance, and cost efficiency and it has been used for instance for the manufacturing of contact lenses and as a lining for artificial hearts.[39–41] In addition to the favorable properties mentioned above, PCL exhibits slower and more controlled biodegradation than other polymers; however, unlike PVA, PCL is highly hydrophobic.[42] PAN is considered a good material for filtering fine dust due to its large dipole moment and has been used for the production of various textile fibers.[43] The initial concentration of PS in the electrospinning solutions of all polymers and the operating parameters applied to the electrospinning process were fixed. To achieve thermal crosslinking of PVA-based scaffolds and to define how the crosslinking affects the material properties, PVA-based NFs containing sebacic acid (**SA**) as crosslinker were also prepared.

FT-IR spectral measurements were used to demonstrate the successful binding of **AsymPc** and cross-linking of PVA with **SA**. All PVA-based NFs exhibited peaks at 3700–3000 cm^{-1} due to

Table 1 Electronic absorption and photophysical data for SymPc and AsymPc

PS solvent	λ_{abs}/nm ($\log_{10}\varepsilon$)	λ_{em}/nm	$\Phi_F{}^a \pm 0.03$	$\Phi_\Delta{}^b \pm 0.03$
SymPcDMF	692 (5.24); 624 (4.55); 323 (4.85)	710	0.08	0.41
SymPcH_2O	680 (4.50); 644 (4.52); 325 (4.74)	n.d.	n.d.	0.26
AsymPcDMF	694 (5.14); 625 (4.52); 326 (4.80)	711	0.11	0.60
AsymPcH_2O	688 (4.64); 650 (4.67); 327 (4.73)	n.d.	n.d.	0.14

[a] Quantum yields were calculated by the steady-state comparative method using zinc phthalocyanine as a reference ($\Phi_F = 0.28$ in DMF). [b] Quantum yields were measured using the relative method using zinc phthalocyanine ($\Phi_\Delta = 0.56$) or methylene blue ($\Phi_\Delta = 0.52$) as a reference. n.d. – not detectable.

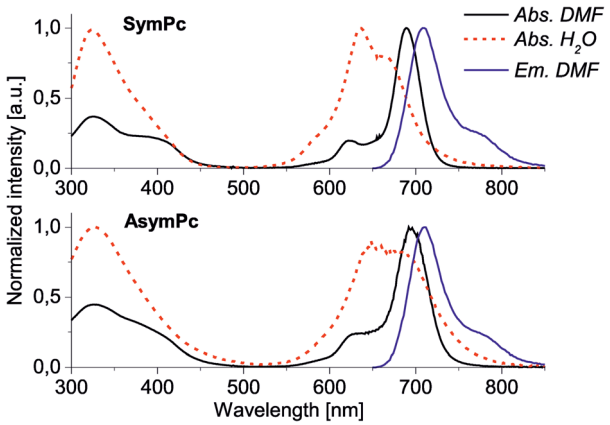

Fig. 2 Normalized UV-vis absorption and emission (λ_{exc} = 610 nm) spectra of **SymPc** (top) and **AsymPc** (bottom) in DMF and H_2O. Molar concentrations were 1×10^{-5} M.

the O–H stretching and 3000–2800 cm^{-1} due to the C–H stretching. As a result of the exceedingly small amount of PS incorporated into the polymer in the FT-IR spectra only weak signals for PS could be observed, making it difficult to distinguish them from the stronger polymer signal. Nevertheless, a peak observed at 1711 cm^{-1} in the spectra of **SymPc + SA PVA**, **AsymPc PVA**, and **AsymPc + SA PVA** were ascribed to C=O stretching of the ester bonds, confirming binding of PS to PVA and/or cross-linking of the PVA with SA. FT-IR spectrum of **SymPc PAN** is dominated by characteristic absorption peak of CN stretch at 2241 cm^{-1} and at 2935 and 1456 cm^{-1} due to the CH_2 groups, whereas the spectrum of **SymPc PCL** showed a very sharp peak at 1722 cm^{-1} due to the C=O stretching mode and a peak around 2943 cm^{-1} corresponds to the O–H groups. This indicates the successful fabrication of the PAN or PCL-based NFs (see ESI†).

Fig. 1 shows the representative scanning electron micrographs (SEM) of the NFs obtained. As could be seen from the micrographs of the as-electrospun materials, randomly oriented and bead-free three-dimensional nanostructures were obtained in all cases. PVA-based NFs showed a very smooth surface with an average fiber diameter of ~350 nm. NFs of **SymPc PAN** also consist of smooth fibers with an average diameter of ~148 nm. The surface of **SymPc PCL** was somewhat rough and with an average diameter of ~1320 nm it showed a significant increase in diameter compared to the other NFs. The reason for this is most likely the tendency of hydrophobic PCL to solidify rapidly in the presence of non-solvents such as water from the environment. It is important to note that the addition of PS or the crosslinker SA had no significant effect on the morphology and fiber diameter of the NFs. SEM images of the bare scaffolds reveal that the average fibre diameters of PVA, PAN and PCL are ~283, ~149 and ~1270 nm, respectively (Fig. S6, ESI†).

Before the determination of the PS content, all NFs were washed with EtOH : H_2O – 7 : 3 mixture followed by H_2O to remove loosely bound PSs. The amount of the PS in the NFs was then estimated *via* UV-vis spectroscopy by dissolving NFs in an appropriate solvent (DMF : H_2O – 1 : 1 for PVA-based scaffolds and DMF for PAN and PCL-based scaffolds) and using calibration curves (Fig. S5a, ESI†). As could be seen from Fig. 3a, the amount of entrapped **SymPc** was comparable in PVA and SA-crosslinked PVA (46.64 and 48.47 nmol mm^{-2}, respectively), while **AsymPc**-containing PVA-based scaffolds had a higher amount of PS (83.93 and 92.77 nmol mm^{-2}, respectively), suggesting that chemical conjugation allows a high degree of drug incorporation. The amount of physically loaded **SymPc** in PAN NF was comparable with the amount of covalently bound **AsymPc** in PVA (93.94 nmol mm^{-2}), however, the amount of **SymPc** in PCL NF was found to be *ca.* sevenfold lower (13.25 nmol mm^{-2}). This difference in PS loading could be explained by the fact that dissolution and diffusion of hydrophilic drugs from highly hydrophobic carrier polymer is very high, due to the tendency of hydrophilic agents to migrate to the surface of the NFs.[43] In contrast, the extent of non-covalent interaction between the PAN and **SymPc** is high, most likely due to the high dipole moment of the polymer. Release kinetics of PS followed by UV-vis in H_2O only showed comparable results (Fig. S5b, ESI†). This demonstrates that different polymeric scaffolds can enhance or inhibit the release of a PS when exposed to aqueous media.

Photosensitized generation of ROS was validated by immersing NFs in an aqueous solution containing ROS-sensitive DCFDA and irradiating them for different periods. In absence of NFs or light, no spectral changes were observed. As shown in Fig. 3b, after light exposure all NFs can sensitize the surrounding oxygen very effectively, and even though the amount of entrapped/bound PS differs, the increase in DCF emission was comparable for all NFs. The binding or conjugation of PSs to polymeric scaffolds can result in the monomerization of PSs reducing aggregation-induced self-quenching in favor of radiative relaxation. Considering the obtained results, we also hypothesize that only the amount of PS present on the

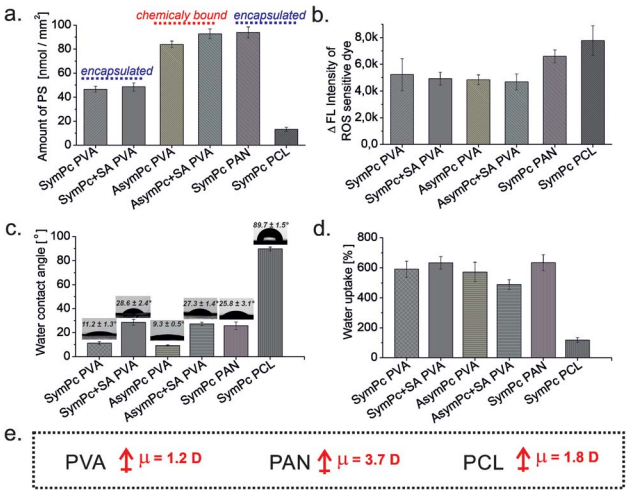

Fig. 3 Characterization of NFs; (a) amount of PS, (b) generation of ROS, (c) water contact angle, (d) water uptake ability of NFs, and (e) dipole moments of the carrier polymers.

surface of the NF scaffold can efficiently induce the oxidation of DCFDA.

The degree of wettability of NFs was assessed and compared through measurement of the contact angle by allowing a single drop of distilled water to stand and spread on the surface for the 30 s. The water contact angles of **SymPc PVA** and **AsymPc PVA** were 11.2 ± 1.3° and 9.3 ± 0.5°, respectively, while for **SymPc + SA PVA** and **AsymPc + SA PVA** the values of 28.6 ± 2.4° and 27.3 ± 1.4° were obtained, showing that additional cross-linking of NFs with SA makes the surfaces of NFs more hydrophobic. While the water contact angle of the **SymPc PAN** with the value of 25.8 ± 3.1° was comparable to the cross-linked PVA samples, a much higher value of 89.7 ± 1.5°was determined for the **SymPc PCL** (Fig. 3c).

Together with wetting dynamics the capacity to absorb water is one of the important characteristics of biomaterials. Owing to the hydrophilic property and the formation of a swollen stable hydrogel, after ~1 h incubation PVA and PAN-based NFs showed a high degree of swelling (489–635%), while the swelling ratio of PCL-based NF (118%) determined under same conditions was significantly low.

2.3 Antibacterial performance

The antibacterial activity of the PSs and NF samples against Gram-negative *E. coli* strain Nissle 1917 and Gram-positive *B. subtilis* strain DB104 were studied, including control experiments that did not contain any PS or NF and non-irradiated samples (dark control). The evaluations were based on the CFU (colony forming units)-counting method. aPDT viability assays of the PSs indicated higher activity of the **SymPc** compared to **AsymPc** against Gram-positive and Gram-negative bacteria in the concentration range of 1 nM to 1 μM. In the dark, either PSs had little or no effect on bacterial growth. When irradiated with light doses of 9 J cm^{-2}, a >3 $\log_{10}$ CFU reduction of Gram-positive *B. subtilis* was achieved with 0.1 μM **SymPc** or 0.5 μM **AsymPc**. Under the same irradiation conditions Gram-negative *E. coli*, the amount of PS required to achieve >3 log10 reduction was 0.5 μM for **SymPc** and 1 μM for **AsymPc** (Fig. S6, ESI†).

Previous studies showed that cell viability could be reduced significantly using materials that contain PS *via* surface attachment,[44,45] or bulk incorporation.[46] The cytotoxic effect of

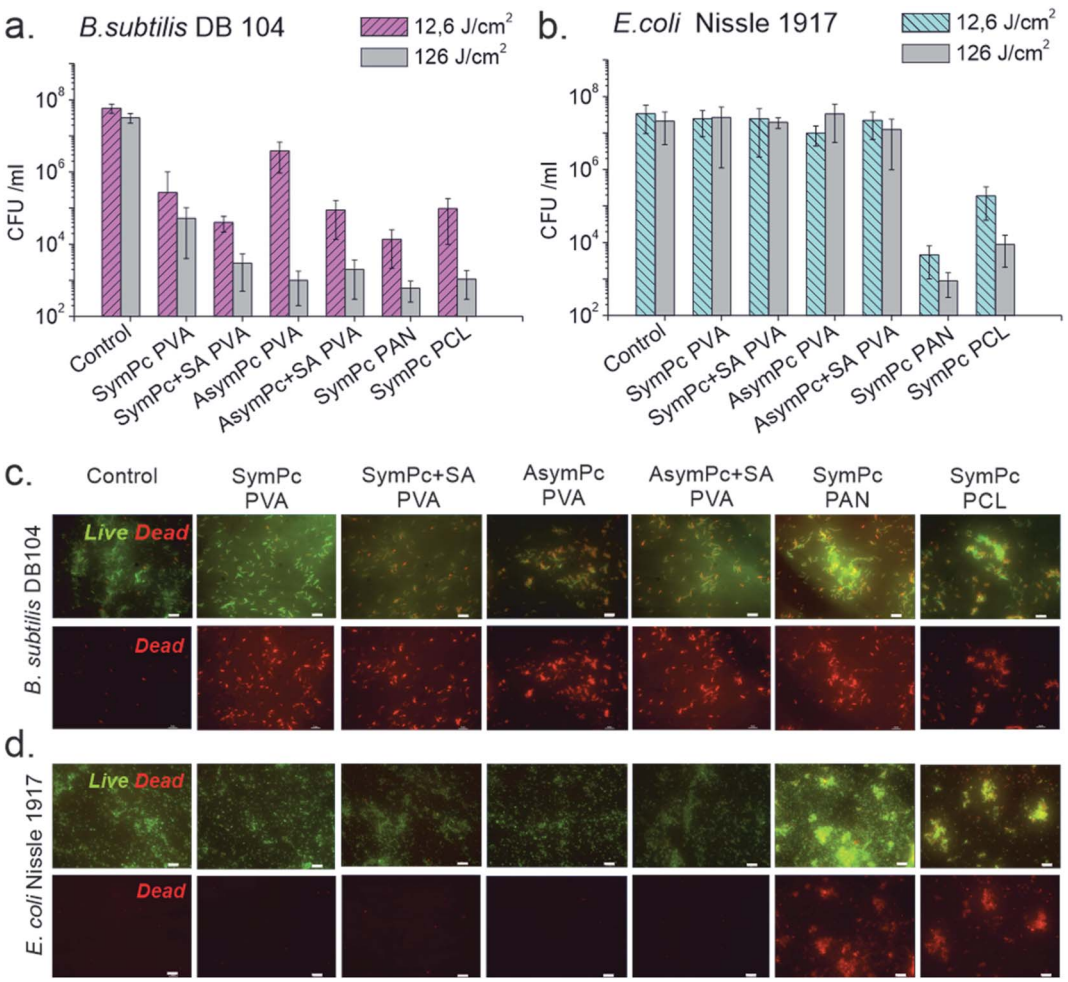

Fig. 4 Viability of *B. subtilis* strain DB104 (a) and *E. coli* strain Nissle 1917 (b) after incubation with corresponding NF for 15 min in dark and irradiation with light doses of 12.6 and 126 J cm^{-2}. Representative fluorescence microscopy images of Live/Dead stained cells of *B. subtilis* DB104 (c) and *E. coli* Nissle 1917 (d) after irradiation with 126 J cm^{-2} light. Scale bar = 10 μm.

the nano-systems based on photodynamic action arises from the ROS generated during irradiation, which can diffuse and non-specifically attack cellular targets in microorganisms and kill them. Although unlike singlet oxygen and hydroxyl radicals, superoxide and peroxide have much longer diffusion lengths and half-lives in the biologically relevant environment,[47] the total diffusion length of the biologically relevant effect is limited, and only microbial cells located in close proximity to NF could be inactivated (Fig. 5a). In this regard, it is important to consider that the carrier polymer can affect the interaction between the microorganisms and the nanomaterial, having a significant impact on the inactivation efficacy of the material. Indeed, comparing the activities of PVA-based scaffolds with regard to *B. subtilis* it becomes evident that at lower irradiation doses (12.5 J cm^{-2}) SA crosslinked probes outperform their non-crosslinked analogs despite the similar loading amount of PS (Fig. 4a). **SymPc PAN** NFs demonstrated higher activity, while the level of inactivation for **SymPc PCL** scaffold was comparable with non-crosslinked PVA-based scaffolds. Nevertheless, at high light doses (125 J cm^{-2}) all NFs showed a significant decrease in the viability of *B. subtilis*. Photoinduced antibacterial susceptibility testing against Gram-negative *E. coli* indicated that only PAN and PCL-based scaffolds could reduce the viability of the cells; none of the PVA-based scaffolds showed any efficacy, even after prolonged irradiation (125 J cm^{-2}, Fig. 4b). To visualize bacterial viability after 125 J cm^{-2} red light irradiation cells were harvested and stained with SYTO 9 (green fluorescence) and propidium iodide (red fluorescence). As shown in Fig. 4c, *B. subtilis* cells display red fluorescence for all NFs, but in the case of *E. coli* red fluorescence could be seen only for bacteria that were incubated with PAN and PCL-based NFs (Fig. 4d). Greater activity of **SymPc PAN** and **SymPc PCL** compared to the PVA-based scaffolds could not be explained based on the differences in the PS content, wettability, and water uptake only. Although it was demonstrated that improvement of the wettability of the surface of electrospun NF material increased its photoinduced antibacterial activity,[48] our current study shows that hydrophobic PCL-based NF was more active against *E. coli* than hydrophilic PVA-based scaffolds regardless of the binding mode and amount of PS. Considering the fact that the proximity of microorganisms to a NF surface is required, it can be assumed that polyvalent interactions between microorganisms and NFs play an important role for materials with a photosensitizing mechanism of action (Fig. 5b). If the hydration layer on NFs is tightly bound, water would have to be withdrawn to make room for a bacterial cell. Such a dehydration process is thermodynamically unfavorable and can lead to cell repellence. Given the high number of hydroxyl groups in PVA, the hydrogen bonding between the water molecule and PVA has a pronounced effect. This explains the overall reduced efficacy of PVA-based NFs. In the classical thermodynamic theory of bacteria–surface interactions explained by extended Derjaguin–Landau–Verwey–Overbeek theory (XDLVO) total interaction force is given by the sum of the electrostatic, the van der Waals, and acid–base interactions.[49] Comparing the dipole moments of PVA, PAN, and PCL (1.2, 3.7, and 1.8 D, respectively) with their photodynamic effects, it could be concluded that the dipole moment could have a profound effect on the interactions between bacteria and NF. Support for this observation comes from the evidence that **SymPc PAN** was found to be more active against both Gram-positive and Gram-negative bacteria, despite the similar PS content and water contact angle as **AsymPc PVA**. As a result of pronounced hydrophobic interactions between bacteria and PCL scaffold, **SymPc PCL** proved to be more active than PVA-based scaffolds despite the small amount of encapsulated PS and a comparable dipole moment of PCL and PVA. These observations clearly show that the overall photodynamic effect of NFs depends not only on the type of bacteria or PS but also on the complex physicochemical structure of the nanomaterials, where hydrodynamic forces might also play an important role.

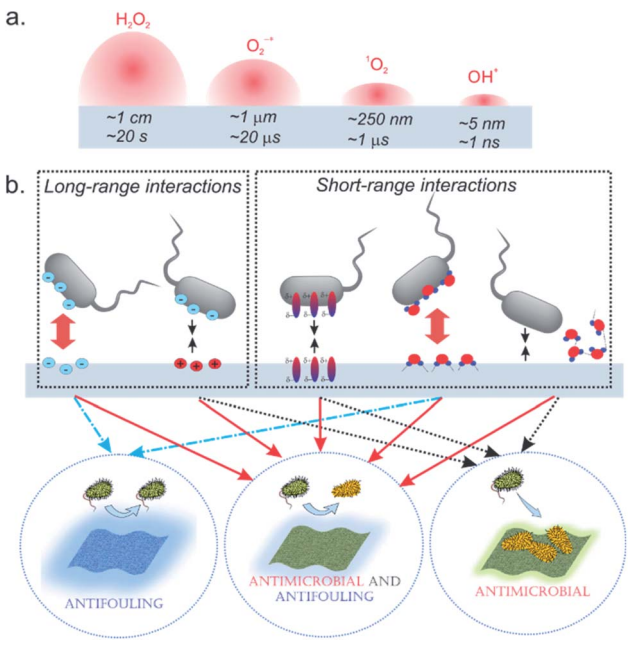

Fig. 5 (a) Relative diffusion and lifetimes of different reactive oxygen species in biologically relevant media (not to scale), (b) diagram summarizing components contributing to XDLVO-based interactions between a bacterium and a surface.

Bacteria-surface interactions are essential not only for photodynamic action but also play a crucial role in biofouling and biofilm formation on various surfaces. For long-term antimicrobial application, the antifouling performance of NFs is essential. Despite the increasing use of NFs in various fields, there are only a few studies that address microbial adhesion to NFs.[50,51] The most prominent strategy to avoid biofouling and biofilm formation is the use of hydrophilic polymers and hydrogels that resist the adhesion of undesired biomaterials due to the formation of the water layer on the surface.[52–54]

This "biopassive" approach is a powerful way to improve material properties avoiding bacterial contamination,[55] however, number of studies indicated that the use of wettability as a surface descriptor is not helpful in understanding bacteria–surface interactions.[56] It has recently been suggested that bacterial elasticity and shape may also govern bacterial

adhesion to substrates.[57] Experiments of microbial biofouling were performed with *B. subtilis* and *E. coli* by immersing NFs in 300 μL bacterial suspensions (approximately 1×10^8 CFU mL^{-1}) in a 48-well plate for 1 h at 37 °C and gently washing NFs with PBS afterwards. Two quantification methods were used to estimate the population of adherent bacteria; measuring the metabolic activity of the cells using XTT-assay and CFU-counting (Fig. S7, ESI†). Comparison of individual methods showed that the XTT-assay underestimated the amount of adherent *E. coli*, however, both methods let us conclude that the adhesion forces of single bacteria are much weaker on PVA and PAN-based NFs than on PCL-based NF. This is in agreement with our previous study, showing that PVA-based NFs demonstrate good antifouling property against *B. subtilis*.[58] PAN-based NFs also demonstrated low fouling values for *B. subtilis*. It should be noted, however, that adhesion of *E. coli* cells to the surfaces was considerably high, since *E. coli* surface structures such as lipopolysaccharides and pili can increase both the initial reversible as well as irreversible attachment to the surface.[59] Regardless of the fiber diameter and the bacterial species used, electrospun NFs made from PCL are known to be highly susceptible to bacterial colonization and biofilm formation.[60] Recently it was shown that PCL-NFs can even detach already formed biofilm from the substrate.[61]

2.4 Antiviral performance

With a much smaller pore size than surgical masks, electrospun materials hold great promise for applications in personal protective equipment as well as air and liquid filtration. The particular advantage of NFs containing PS is not only the trapping of viral aerosols but also the light-triggered inactivation of the trapped pathogens. The antiviral efficacy of NFs was evaluated using bacteriophages as surrogates because they are rapidly and relatively easy to detect, lack human pathogenicity, and respond to photodynamic effect in a similar way as mammalian viruses.[62] Two different viral models were used to assess the efficacy of PSs and NFs. The phi6 bacteriophage, an enveloped dsRNA virus used as a surrogate for enveloped viruses including SARS CoV-2 (that caused COVID-19 Pandemic) and Ebola virus. The bacteriophage MS2, a non-enveloped ssRNA virus was used as a model system for human non-enveloped RNA viruses and as a common strain that was used to evaluate the performance of membrane filtration. To quantify the antiviral activity of NFs and PSs, samples were incubated with the bacteriophages suspended in PBS and plaque-forming units (PFU mL^{-1}) were determined by the double layer agar plaque assay after exposure to light.

As shown in Fig. 6a, PVA-based NFs were able to reduce phi6 viability by >3 log_{10} units (99.9%) compared to the dark control when high light doses were used (63 J cm^{-2}), yet inactivation of ~1.5 log_{10} units of light control was also observed under the same irradiation conditions. In contrast, MS2 proved to be less sensitive to aPDT treatment with PVA-based NFs. In this case, the controls showed statistically insignificant differences. Both **SymPc PAN** and **SymPc PCL** showed a significant decrease of phi6 and MS2 phage counts under low light irradiation (18 J cm^{-2}) and reached detection limit (>5 log_{10} units, 99.999%) after irradiation with high light doses (63 J cm^{-2}, Fig. 6a). Interestingly, when PS was used exclusively, the reduction in PFU mL^{-1} after irradiation (6 J cm^{-2}) was lower for phi6 compared to MS2, especially for **AsymPc** (Fig. S9, ESI†). The low level of photodynamic inactivation of phi6 was unexpected, as it is generally assumed that enveloped viruses are more sensitive to photodynamic action compared to non-enveloped viruses.[64] Nevertheless, it should be taken into account that viruses interact with PSs by electrostatic and hydrophobic forces. Enveloped viruses such as phi6 are highly sensitive to lipid bilayer disruption, and dyes that are primarily lipophilic, such as merocyanin 540, have been shown to be very efficient at viral inactivation.[63] On the other hand, it known that the inactivation of MS2 is caused by damage to its A protein by exogenous singlet oxygen.[64,65] Positively charged PSs such as **SymPc** and **AsymPc** can interact very efficiently with MS2, leading to its rapid inactivation upon irradiation. The specific electrostatic and hydrophobic properties of the phages are also important for the interaction with NFs with different hydrophobicities and charges. This can explain differences in inactivation tendency and kinetics of phi6 and MS2 when NFs were used.

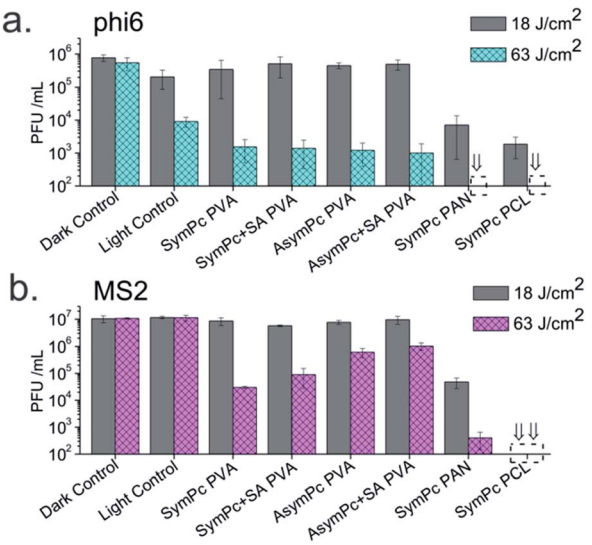

Fig. 6 Survival curves of bacteriophages phi6 (a) and MS2 (b) photoinactivated by nanofibers.

2.5 Biocompatibility of nanofiber scaffolds

Biocompatibility is one of the key requirements for the use of materials and devices in the biomedical and environmental fields. To determine the cytotoxicity of NFs, *in vitro* cell viability studies were performed using cultured human dermal fibroblasts (HDF). Cells were incubated with the corresponding NF and irradiated with 35 W cm^{-2} (125 J cm^{-2}) for 1 hour After that cell viability was determined after 24 hours using the Alamar Blue Viability Assay. As can be seen from Fig. 7a, cell viability did not significantly change under the applied conditions when PVA- and PAN-based NFs were used, but an almost complete loss of cell viability was observed for PCL-based scaffold.

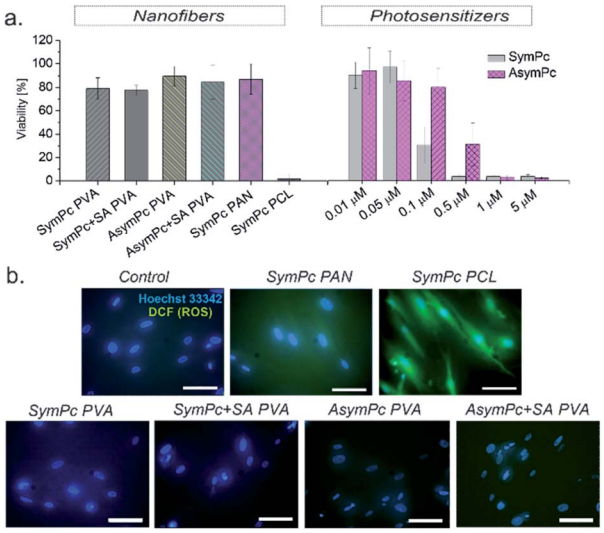

Fig. 7 (a) Viability of HDF cells incubated with NFs or different concentrations of **SymPc** or **AsymPc**, (b) representative fluorescence images DFCDA and Hoechst labeled cells incubated with different NFs and irradiated for 1 h, 35 mW cm^{-2}. Scale bar = 50 μm.

Though before the irradiation experiments we toughly washed NFs to limit the aPDT action to NFs only, diffusion of encapsulated PS could not be excluded. To clarify whether the nanomaterial itself reduced cell viability or the PS released from the NF was the reason, NFs were removed before the irradiation and cells were stained with DCFDA probe to detect the ROS generation. As can be seen in the representative fluorescence images (Fig. 7b), a remarkable green fluorescence signal from DCF was detected only for the cells incubated with **SymPc PCL**, indicating the generation of intracellular ROS upon irradiation. These results imply that a sufficient amount of PS was released from **SymPc PCL** and taken up by the cells. Due to the presence of salts and proteins in the cell culture media, it is likely that a replacement of the already loosely bound PS occurs during incubation.

3. Conclusions

In this manuscript, we describe the fabrication of advanced photoactive nanomaterials that can trap and inactivate microorganisms providing an effective strategy to prevent the spread of pathogenic bacteria and viruses. Nanofibrous PVA-, PAN- and PCL-based materials containing entrapped or covalently bound zinc phthalocyanines as photoactive dyes were prepared. Supported by a series of characterisations, obtained results showed that the molecular and physical properties of the carrier polymers play a more important role in the overall activity of the materials than the concentration and binding mode of the PS. Long-range electrostatic interactions derived from positively charged PS do have a contribution in the initial phase, but since the oxidation effect of the photogenerated free radicals is limited to a few nanometres, the overall antimicrobial effect is dependent on the short-range interactions between microorganism and nanomaterials. Thus, PVA-based scaffolds that form a strong hydration layer proved to be less effective than PAN- and PCL-based nanomaterials, where dipole–dipole or hydrophobic interactions correspondingly dominate. This remarkable observation provides a holistic understanding of the individual contributions to material properties and points to the possibility of producing photoactive, low fouling materials by hitting the right parameters. The high efficacy of photoactive nanomaterials and the possibility of their production on an industrial scale promise a bright future for biocompatible and reusable scaffolds in the medical and technical fields.

4. Experimental

4.1 General

All solvents and chemicals were purchased from Fisher Scientific, TCI, Sigma-Aldrich, Acros Organics or Alfa Aesar and used without further purification. Column chromatography was carried out on silica gel 60 (0.063–0.2 mm) and TLC on aluminium sheets pre-coated with silica gel 60 F_{254}. Mass spectra were measured on the devices Autoflex Speed and MicroOTof ESI (Bruker Daltonics, Bremen, Germany). NMR spectra were measured on Bruker AV 400 (Bruker Corporation, Billerica, Massachusetts, USA) and were analysed using the MestReNova 12.0 program (Mestrelab Reasearch S. L., Santiago de Compostela, Spain). Absorption spectra were measured on an Agilent 8453 spectrophotometer (Agilent Technologies, Inc, Santa Clara, California, USA) and were background corrected. Steady-state emission spectra were recorded on a JASCO FP-8500 fluorescence spectrometer (JASCO Deutschland GmbH, Pfungstadt, Germany) or an Infinite 200 Pro M Plex multi-mode microplate reader (Tecan Group Ltd., Zürich, Switzerland). Electrospinning was done using electrospinner NFES-100 (Micro&Nano Tools, Niagara Falls, Canada). SEM images were taken by HITACHI SU8230 scanning electron microscope (Hitachi Ltd. Corporation, Tokyo, Japan). FT-IR spectra were measured on a Bruker IFS 55 Fourier transform infrared spectrometer (Bruker Corporation, Billerica, Massachusetts, USA). Contact angles were measured with a pendant drop tensiometer DSA100 (Krüss, Hamburg, Germany). Fluorescence microscopy images were recorded on a Nikon inverted microscope TS2R (Nikon Corporation, Tokyo, Japan) equipped with an IS-DMK33UX174 monochrome camera and a LED filter block. A schematic representation of the overall pathways and procedures for the synthesis of the photosensitizers can be found in the ESI.†

4.2 Singlet oxygen quantum yields of PS

Measurements were done as published before.[66,67]

4.3 Electrospinning

All NFs were spun with the same parameters: two 10 mL syringes with metal needles 20G, a voltage of 15 kV, a flow rate of 1.2 mm h^{-1}, a distance of 15 cm, and a rotation speed of the collector 500 rpm. For PVA-based NFs PVA (2 g, M_W 146.000–186.000) was dissolved in H_2O (20 mL) and stirred at 90 °C overnight. After cooling to RT mixture of corresponding ZnPc

(0.02 mmol) and SA (404.0 mg, 2.00 mmol) in DMF (3.5 mL) was added to the solution. Obtained mixture was stirred at 90 °C for 1 h, cooled and then electrospun. After electrospinning NFs were heated at 120 °C for 1 h. SymPc-PAN was obtained by electrospinning solution of PAN (2 g, M_W 150.000) and SymPc (31.6 mg, 0.02 mmol) in DCM and SymPc-PCL was obtained by electrospinning solution of PCL (2 g, M_W 80.000) and SymPc (31.6 mg, 0.02 mmol) in DMF : THF 1 : 1.

4.4 Scanning electron microscopy measurements

To perform SEM measurements, the samples were sputter-coated with Ag and imaged with an accelerating voltage using Zeiss SmartSEM software. Image j (NIH) (Bethesda, MD) was used to determine the diameter of the fibers in the NFs.

4.5 Determination of photosensitizers concentration in NFs

UV-Vis spectroscopy was used to determine the PS loading. To obtain a constant area of approximately 113 cm^2, samples were randomly cut from the mat at different locations using a 12 cm diameter hole punch. The samples were washed with 70% ethanol solution (1 × 1 mL) and water (3 × 1 mL) to remove unbound PS and then heated at 100 °C for 1 h in a 1 mL DMF–H_2O 1 : 1 mixture in case of PVA-based NFs and in DMF for PAN and PCL based NFs.

4.6 Singlet oxygen detection for NFs

NFs were places in 24 well plates and of 300 μL DCFDA solution was added. After irradiation for defined time (10 to 280 s), 100 μL of solution was taken and replaced in microplate and emission was measured.

4.7 *In vitro* swelling study

Water absorption capacities of the prepared scaffolds were determined by immersing a square piece (12 mm diameter) of NF in water at room temperature. Once the equilibrium was reached (~1 h), the samples were removed and the surface wetness was removed using filterpaper. The following equation as used to calculate the equilibrium-swelling ratio

$$\text{Swelling}(\%) = \left(\frac{W_i - W_f}{W_i}\right) \times 100$$

where W_i and W_f are the initial and final weight of the scaffold, respectively.

4.8 Bacterial strains and culture conditions

B. subtilis strain DB104 and *E. coli* strain Nissle 1917 were grown on lysogeny broth (LB) agar and kept at 4 °C. A single isolated colony was picked from this plate, transferred to 3 mL LB broth, and incubated aerobically overnight at 37 °C in a shaker incubator at 180 rpm (rotations per minute). The following day, bacteria were suspended in 10 mL of fresh LB medium to an optical density $OD_{600} = 0.1$ and grown in a flask to an attenuation of approximately $OD_{600} = 0.4$. Thereafter, the bacterial suspensions were centrifuged at 4000 rpm for 5 min, resuspended in a buffer solution to the final bacterial concentration of approximately 1×10^{-8} cells per mL, and used for the experiments.

4.9 Photoinactivation of bacteria

For the irradiation experiments, 1 mL of PS-stained bacteria (15 min, 37 °C) was placed in a 24-well plate and irradiated with an LED lamp (660 ± 24 nm) for a certain duration. A power meter (Solar Meter from Solartech) was used to measure fluence rates regularly. After irradiation, viable bacterial cells were determined by serial dilutions of the bacterial suspension plated on Luria–Bertani agar plates. The number of CFU ml^{-1} was calculated using a ProtoCOL automatic colony counter from Synbiosis. The same method was used for NFs. Beforehand, NFs were treated with 70% aqueous ethanol solution for 1 h and then washed with a sufficient amount of PBS to disinfect them and remove unbound PSs. Each Ø 12 mm NF was incubated with approximately 200 μL bacterial suspension for 15 min before irradiation.

4.10 Quantification of bacteria adherent on NFs

Ø 12 mm pre-sterilized and washed NFs were immersed in the 200 μL bacterial suspension (*ca.* 1 × 10-8 cells per mL) in a 24-well plate under static conditions at 37 °C for 1 h and were washed carefully with PBS afterwords. For the determination of viable cells, two methods were used; (i) XTT assay, based on the reduction of 2,3-bis(2-methoxy-4-nitro-5-sulfophenyl)-5-[(phenylamino)carbonyl]-2*H*-tetrazolium hydroxide (XTT) in the metabolically active microbial cells to a water-soluble formazan. 200 μL of XTT-menadione solution was prepared as described previously[68] and added to NFs. After incubation for 7 h an aliquot of 100 μL was then taken, transferred to a 96-well plate and absorbance was recorded at 492 nm with a microplate reader (Tecan, Switzerland). The results were expressed as the relative viability (% control). (ii) for CFU mL^{-1} determination NFs were places in vials, 200 μL PBS was added and the probes were sonicated for 5 min. The number of viable bacteria was counted by serial dilutions of the bacterial suspension plated on Luria–Bertani agar plates.

4.11 Virus strains and methods

Stocks of bacteriophages phi6 DSM 21518 and MS2 DSM 13767 and the corresponding host cells *Pseudomonas syringae* van Hall 1902 DSM-21482 and *Escherichia coli* DSM-5695 were purchased from DSMZ Germany. Propagation was carried out according to the specifications provided by the Leibniz Institute DSMZ-German Collection of Microorganisms and Cell Cultures GmbH (Braunschweig, Germany). Photodynamic inactivation of bacteriophages phi6 and MS2 was investigated using prewashed and sterilized NFs or a range of concentrations of SymPc and AsymPc 31.3 nM to 500 nM in PBS. Double layer agar plaque assays were carried out before and after irradiation to determine the extent of phage inactivation.

Cell line, growth condition and *in vitro* viability assay. Human Dermal Fibroblasts (HDF adult, Sigma Aldrich) was cultured in cell Roswell Park Memorial Institute (RPMI 1640) medium, supplemented with 1% (v/v) penicillin/streptomycin,

2% L-glutamine, and 10% (v/v) fetal bovine serum (FBS) at 37 °C in a humidified 5% CO_2 incubator. When cells reached 70–90% confluence, they were detached from the surface using trypsin/EDTA. About 2×10^4 cells per well in the medium were incubated in 96-well plates and allowed to adhere overnight. For the experiments 0.01–5 μM photosensitizer or Ø 3 mm sterilized NFs were used. Cells with PS or NFs were incubated for 1 h at 37 °C in the dark; subsequently, the medium was discarded and/or NFs removed and replaced with a new medium followed by irradiation of 1 h. Cell viability was assessed using Alamar Blue assay. After irradiation, the cells were incubated at 37 °C under 5% CO_2 for 24 h. The medium was replaced with 200 μL of 10% Alamar Blue (Sigma) solution in growth medium followed by incubation for 7 h. The plate was shaken on a microplate reader (Tecan, Switzerland) for 20 s before the fluorescence at each well was measured (E_x 535 nm/E_m 595 nm). The viability of HDF cells was then expressed as the relative viability (% control).

4.12 Staining with ROS sensitive dye

Cultures of HDF cells were incubated with Ø 3 mm NFs that were sterilized as described above for the NFs used in antibacterial and antiviral studies using EtOH/H_2O. Prior irradiation cells were stained with 2′,7′-dichlorofluorescein diacetate for 5 min. After being exposed to red light irradiation with 35 mW cm^{-2} for 1 h (127 J cm^{-2}) HDF cells were stained with Hoechst 33342 according to manufacturer's instructions. The cell nucleus was selectively excited with light at 338/390 nm filter and emission was recorded through a 475/490 nm filter. For the detection of DCF filters a 440/470 nm filter was used for excitation and 534/555 nm filter for detecting emission.

4.13 Statistical analysis

Data are expressed as mean ± standard deviation. Student's *t*-test and one-way analysis of variance within groups were used to compare the treatment effects. $p < 0.05$ was considered to represent a significant difference.

Author contributions

A. G. conceived, planned and carried out all experiments, analysed data and wrote the manuscript. H. M. contributed to the experiments with microphages U. D. provided the bacterial strains. H. M and U. D. contributed to the final version of the manuscript.

Conflicts of interest

The authors declare no competing financial interest.

Acknowledgements

This work was supported by the Deutsche Forschungsgemeinschaft (grant GA 2362/2-1 to A. G.), Fonds der Chemischen Industrie and WWU Münster Internationalisation Fund. We acknowledge support from the Open Access Publication Fund of the University of Münster.

References

1 Q. Yu, Z. Wu and H. Chen, *Acta Biomater.*, 2015, **16**, 1–13.
2 J. Bruenke, I. Roschke, S. Agarwal, T. Riemann and A. Greiner, *Macromol. Biosci.*, 2016, **16**, 647–654.
3 J. Song, M. Chen, M. B. Olesen, C. Wang, R. Havelund, Q. Li, E. Xie, R. Yang, P. Boggild, C. Wang, F. Besenbacher and M. Dong, *Nanoscale*, 2011, **3**, 4966–4971.
4 D.-N. Phan, N. Dorjjugder, M. Q. Khan, Y. Saito, G. Taguchi, H. Lee, Y. Mukai and I.-S. Kim, *Cellulose*, 2019, **26**, 6629–6640.
5 J. L. Castro Mayorga, M. J. Fabra Rovira, L. Cabedo Mas, G. Sanchez Moragas and J. M. Lagaron Cabello, *J. Appl. Polym. Sci.*, 2018, **135**, 45673.
6 B. I. Kharisov, H. V. R. Dias, O. V. Kharissova, V. M. Jimenez-Perez, B. Olvera Perez and B. Munoz Flores, *RSC Adv.*, 2012, **2**, 9325–9358.
7 N. M. Bedford and A. J. Steckl, *ACS Appl. Mater. Interfaces*, 2010, **2**, 2448–2455.
8 J. J. Harrison, H. Ceri and R. J. Turner, *Nat. Rev. Microbiol.*, 2007, **5**, 928–938.
9 M. R. Wiesner, G. V. Lowry, P. Alvarez, D. Dionysiou and P. Biswas, *Environ. Sci. Technol.*, 2006, **40**, 4336–4345.
10 P. Elena and K. Miri, *Colloids Surf., B*, 2018, **169**, 195–205.
11 Y. Jiao, L.-n. Niu, S. Ma, J. Li, F. R. Tay and J.-h. Chen, *Prog. Polym. Sci.*, 2017, **71**, 53–90.
12 S. Buffet-Bataillon, P. Tattevin, M. Bonnaure-Mallet and A. Jolivet-Gougeon, *Int. J. Antimicrob. Agents*, 2012, **39**, 381–389.
13 A. Galstyan, *Chem.–Eur. J.*, 2021, **27**, 1903–1920.
14 M. Q. Mesquita, C. J. Dias, M. G. P. M. S. Neves, A. Almeida and M. A. F. Faustino, *Molecules*, 2018, **23**, 1–47.
15 A. Greiner and J. H. Wendorff, *Angew. Chem., Int. Ed.*, 2007, **46**, 5670–5703.
16 J. Xue, J. Xie, W. Liu and Y. Xia, *Acc. Chem. Res.*, 2017, **50**, 1976–1987.
17 J. Xue, T. Wu, Y. Xia, Y. Dai and Y. Xia, *Chem. Rev.*, 2019, **119**, 5298–5415.
18 Z. Zhang, D. Ji, S. Ramakrishna and H. He, *Mater. Sci. Eng., R*, 2021, **143**, 100594.
19 S. Sundarrajan, K. L. Tan, S. H. Lim and S. Ramakrishna, *Procedia Eng*, 2014, **75**, 159–163.
20 P. Lu, S. Murray and M. Zhu, in *Electrospinning: Nanofabrication and Applications*, ed. B. Ding, X. Wang and J. Yu, Elsevier Inc., 2019, pp. 695–717.
21 Y. Dou, W. Zhang and A. Kaiser, *Adv. Sci.*, 2020, 7, 1902590.
22 Y. Wu, C. Chen, Y. Jia, J. Wu, Y. Huang and L. Wang, *Appl. Energy*, 2018, **210**, 167–181.
23 C. Liu, P.-C. Hsu, H.-W. Lee, M. Ye, G. Zheng, N. Liu, W. Li and Y. Cui, *Nat. Commun.*, 2015, **6**, 6205.
24 M. Mukherjee and S. De, *Environ. Sci.: Water Res. Technol.*, 2018, **4**, 1078–1104.
25 S. Fahimirad, Z. Fahimirad and M. Sillanpaa, *Sci. Total Environ.*, 2021, **751**, 141673.

26 M. Rahmati, D. K. Mills, A. M. Urbanska, M. R. Saeb, J. R. Venugopal, S. Ramakrishna and M. Mozafari, *Prog. Mater. Sci.*, 2021, **117**, 100721.
27 I. Jun, H.-S. Han, J. R. Edwards and H. Jeon, *Int. J. Mol. Sci.*, 2018, **19**, 745/741.
28 A. Hasan, S. Soliman, F. El Hajj, Y.-T. Tseng, H. C. Yalcin and H. E. Marei, *Sci. Rep.*, 2018, **8**, 1–13.
29 G. Sandri, S. Rossi, M. C. Bonferoni, C. Caramella and F. Ferrari, *From Therapeutic Dressings and Wound Healing Application*, John Wiley & Sons Ltd., 2020.
30 Y. Liu, T. Li, Y. Han, F. Li and Y. Liu, *Curr. Opin. Biomed. Eng.*, 2021, **17**, 100247.
31 S. L. Levengood, A. E. Erickson, F.-c. Chang and M. Zhang, *Curr. Opin. Biomed. Eng.*, 2017, **5**, 1822–1833.
32 Y. Gao, Y. B. Truong, Y. Zhu and I. L. Kyratzis, *J. Appl. Polym. Sci.*, 2014, **131**, 40797/40791.
33 C. Blaszykowski, S. Sheikh and M. Thompson, *Chem. Soc. Rev.*, 2012, **41**, 5599–5612.
34 S. Chen, L. Li, C. Zhao and J. Zheng, *Polymer*, 2010, **51**, 5283–5293.
35 S. Jiang and Z. Cao, *Adv. Mater.*, 2010, **22**, 920–932.
36 Q. Wei, T. Becherer, S. Angioletti-Uberti, J. Dzubiella, C. Wischke, A. T. Neffe, A. Lendlein, M. Ballauff and R. Haag, *Angew. Chem., Int. Ed.*, 2014, **53**, 8004–8031.
37 A. Galstyan, D. Block, S. Niemann, M. C. Gruener, S. Abbruzzetti, M. Oneto, C. G. Daniliuc, S. Hermann, C. Viappiani, M. Schaefers, B. Loeffler, C. A. Strassert and A. Faust, *Chem.–Eur. J.*, 2016, **22**, 5243–5252.
38 M. A. Revuelta-Maza, E. de las Heras, M. Agut, S. Nonell, T. Torres and G. de la Torre, *Chem.–Eur. J.*, 2021, **27**, 4955–4963.
39 E. Chiellini, A. Corti, S. D'Antone and R. Solaro, *Prog. Polym. Sci.*, 2003, **28**, 963–1014.
40 M. Chaouat, C. Le Visage, W. E. Baille, B. Escoubet, F. Chaubet, M. A. Mateescu and D. Letourneur, *Adv. Funct. Mater.*, 2008, **18**, 2855–2861.
41 M. Teodorescu, M. Bercea and S. Morariu, *Biotechnol. Adv.*, 2019, **37**, 109–131.
42 A. Szentivanyi, T. Chakradeo, H. Zernetsch and B. Glasmacher, *Adv. Drug Delivery Rev.*, 2011, **63**, 209–220.
43 A. Kausar, *J. Plast. Film Sheeting*, 2019, **35**, 295–316.
44 B. L. Carpenter, F. Scholle, H. Sadeghifar, A. J. Francis, J. Boltersdorf, W. W. Weare, D. S. Argyropoulos, P. A. Maggard and R. A. Ghiladi, *Biomacromolecules*, 2015, **16**, 2482–2492.
45 D. R. Alvarado, D. S. Argyropoulos, F. Scholle, B. S. T. Peddinti and R. A. Ghiladi, *Green Chem.*, 2019, **21**, 3424–3435.
46 S. L. Stanley, F. Scholle, J. Zhu, Y. Lu, X. Zhang, X. Situ and R. A. Ghiladi, *Nanomaterials*, 2016, **6**, 77/71.
47 M. Levy, P. P. Chowdhury, P. Nagpal, M. Levy, P. P. Chowdhury, P. Nagpal and P. Nagpal, *J. Biol. Eng.*, 2019, **13**, 48.
48 P. Henke, H. Kozak, A. Artemenko, P. Kubat, J. Forstova and J. Mosinger, *ACS Appl. Mater. Interfaces*, 2014, **6**, 13007–13014.
49 Y. Cheng, G. Feng and C. I. Moraru, *Front. Microbiol.*, 2019, **10**, 191.
50 S. Lencova, V. Svarcova, H. Stiborova, K. Demnerova, K. Zdenkova, V. Jencova and K. Hozdova, *ACS Appl. Mater. Interfaces*, 2021, **13**, 2277–2288.
51 F. De Cesare, E. Di Mattia, E. Zussman and A. Macagnano, *Environ. Sci.: Nano*, 2019, **6**, 778–797.
52 K. L. Prime and G. M. Whitesides, *Science*, 1991, **252**, 1164–1167.
53 S. Lowe, N. M. O'Brien-Simpson and L. A. Connal, *Polym. Chem.*, 2015, **6**, 198–212.
54 A. Hucknall, S. Rangarajan and A. Chilkoti, *Adv. Mater.*, 2009, **21**, 2441–2446.
55 H. J. Busscher, d. M. H. C. van, G. Subbiahdoss, P. C. Jutte, d. D. J. J. A. M. van, S. A. J. Zaat, M. J. Schultz and D. W. Grainger, *Sci. Transl. Med.*, 2012, **4**, 153rv110.
56 A. L. Hook, J. Yang, M. C. Davies, M. R. Alexander, C.-Y. Chang, J. Luckett, A. Cockayne, S. Atkinson, P. Williams, Y. Mei, R. Langer, D. G. Anderson, R. Bayston, D. J. Irvine, R. Langer, D. G. Anderson, R. Langer and D. G. Anderson, *Nat. Biotechnol.*, 2012, **30**, 868–875.
57 L. Tamayo, F. Melo, L. Caballero, E. Hamm, M. Diaz, M. S. Leal, N. Guiliani and M. D. Urzua, *ACS Appl. Mater. Interfaces*, 2020, **12**, 14507–14517.
58 K. Strokov, A. H. Schaefer, U. Dobrindt and A. Galstyan, *ACS Appl. Bio Mater.*, 2020, **3**, 3751–3760.
59 R. Van Houdt and C. W. Michiels, *Res. Microbiol.*, 2005, **156**, 626–633.
60 J. A. Tamayo-Ramos, C. Rumbo, F. Caso, A. Rinaldi, S. Garroni, A. Notargiacomo, L. Romero-Santacreu and S. Cuesta-Lopez, *ACS Appl. Mater. Interfaces*, 2018, **10**, 32773–32781.
61 C. Rumbo, J. A. Tamayo-Ramos, M. F. Caso, A. Rinaldi, L. Romero-Santacreu, R. Quesada and S. Cuesta-Lopez, *ACS Appl. Mater. Interfaces*, 2018, **10**, 11467–11473.
62 L. Costa, M. A. F. Faustino, M. G. P. M. S. Neves, A. Cunha and A. Almeida, *Viruses*, 2012, **4**, 1034–1074.
63 C. D. Lytle, A. P. Budacz, E. Keville, S. A. Miller and K. N. Prodouz, *Photochem. Photobiol.*, 1991, **54**, 489–493.
64 H. Majiya, O. O. Adeyemi, M. Herod, N. J. Stonehouse and P. Millner, *J. Photochem. Photobiol., B*, 2018, **189**, 87–94.
65 H. Majiya, O. O. Adeyemi, N. J. Stonehouse and P. Millner, *J. Photochem. Photobiol., B*, 2018, **178**, 404–411.
66 A. Galstyan, A. Ricker, H. Nuesse, J. Klingauf and U. Dobrindt, *ACS Appl. Bio Mater.*, 2020, **3**, 400–411.
67 K. Strokov and A. Galstyan, *Eur. J. Org. Chem.*, 2020, **2020**, 7327–7332.
68 A. Galstyan, R. Schiller and U. Dobrindt, *Angew. Chem., Int. Ed.*, 2017, **56**, 10362–10366.